Electrical anisotropy and coexistence of structural transitions and superconductivity in IrTe₂

Guixin Cao,[1] Weiwei Xie,[2] W. Adam Phelan,[1] J. F. DiTusa,[1] and Rongying Jin[1,*]

[1]*Department of Physics and Astronomy, Louisiana State University, Baton Rouge, Louisiana 70803, USA*
[2]*Department of Chemistry, Louisiana State University, Baton Rouge, Louisiana, 70803, USA*

We report experimental investigations of the electrical transport, magnetic, and thermodynamic properties of IrTe₂ single crystals. The resistivity, magnetization, and specific heat display anomalies at $T_{S1} \approx 283$ K, $T_{S2} \approx 167$ K, and $T_c \approx 2.5$ K, corresponding to two structural and one superconducting phase transitions, respectively, demonstrating the coexistence of all of these transitions in high-quality stoichiometric samples. While there is little magnetic anisotropy, a large ab-plane (ρ_{ab}) and c-axis (ρ_c) electrical resistivity ratio ($\rho_c/\rho_{ab} \approx 730$ at $T = 4$ K) is observed. This two-dimensional (2D) electronic character is further reflected in the disparate temperature dependences of ρ_{ab} and ρ_c, with ρ_{ab} exhibiting a Fermi-liquid-like T^2 dependence below ~25 K, while ρ_c deviates significantly from this standard metallic behavior. In contrast, the magnetization is almost isotropic and negative over a wide temperature range. This can be explained by larger diamagnetism induced by electronic structure reconstruction as probed by the Hall effect and smaller positive contribution from itinerant electrons due to a low density of states (DOS) at the Fermi level. A small electronic specific heat coefficient with $\gamma \approx 1.8$ mJ/mol K² confirms this assertion. This implies that IrTe₂ is a weakly coupled superconductor. The connection between the superconductivity and the two structural transitions is discussed.

I. INTRODUCTION

The unusual and complex structural and physical properties of layered transition metal dichalchogenides have been investigated for many years. Two of the most frequently observed phenomena are charge density wave (CDW) instabilities and superconductivity. While a CDW is often formed in low-dimensional systems, bulk superconductivity will display a three-dimensional character. Thus, they are considered incompatible in a conventional sense. This is indeed the case in many transition metal dichalchogenides, where superconductivity emerges as the CDW transition is suppressed by chemical doping or applied pressure [1–3]. However, there is evidence for the coexistence of CDW and superconductivity in some compounds suggesting a causal relationship [4–7]. Reconciling these two viewpoints is a key issue for the condensed matter physics community, because elucidating the connections between superconductivity and CDW instabilities as well as understanding what role CDW fluctuations play in the formation of unconventional superconducting phases is crucial to an understanding of the prevalence of superconductivity in two-dimensional materials.

The formation of a CDW is usually accompanied by a lattice distortion, so that the observation of a structural modulation at $T_{S1} \approx 283$ K in IrTe₂ is thought to originate from a CDW instability [8]. Furthermore, the suppression of T_{S1} by chemical doping is accompanied by the emergence of superconductivity [8–12], suggesting that the structural phase transition/CDW and superconductivity are incompatible. However, the first-order [7,8] and nonsinusoidal structural transition [13] with the absence of an energy gap [12,14,15] put the CDW scenario at T_{S1} in doubt. This set of experimentally established facts taken as a whole is confusing such that the rich structural and physical properties of IrTe₂ are unsettled. For example,

IrTe₂ has been found to crystallize at room temperature in either trigonal ($P\bar{3}m1$) [16] or cubic ($Pa\bar{3}$) symmetry [17,18] at ambient pressure, while high-pressure synthesis yields a monoclinic ($C2/m$) symmetry [19]. Trigonal IrTe₂ has been found to undergo one structural phase transition at T_{S1} in some reports [8,12,16,20] and two structural phase transitions in other reports at T_{S1} and T_{S2}, with T_{S2} in the range of 150–180 K [21,22]. Below T_{S1}, both the monoclinic [16] and triclinic [20,23] structures have been reported. According to Ref. [21], the transition at T_{S2} can only be observed in high-quality samples. These different structure types yield very different physical properties so that a unified picture of the IrTe₂ system has yet to be developed.

Here, we report the structural, electrical, magnetic, and thermodynamic properties of IrTe₂ single crystals. These investigations indicate that the system undergoes three consecutive phase transitions, i.e., two structural transitions at high temperature and a superconducting transition at a lower temperature. While magnetic properties reveal a three-dimensional character, the electrical resistivity exhibits an extremely high anisotropy. In addition, our Hall-effect measurements indicate a small carrier concentration for all temperatures and fields investigated, with a significant Fermi surface reconstruction apparent at both T_{S1} and T_{S2}. The observation of superconductivity in our crystals below 2.5 K along with an increased apparent Hall carrier density for $T < T_{S2}$ suggest that the higher carrier density may be necessary for the nucleation of superconductivity in IrTe₂. This observation may be a key to understanding the role of chemical substitution and the apparent sample quality dependence in the nucleation of superconductivity.

II. EXPERIMENTAL DETAILS

Large IrTe₂ single crystals were grown using the self-flux method described previously [12,23]. The resulting shiny platelike single crystals have a triangular-shaped surface and

---

*Corresponding author: rjin@lsu.edu

TABLE I. Single-crystal crystallographic data for IrTe$_2$ at 300 and 250 K.

Refined formula	IrTe$_2$	IrTe$_2$
Temperature (K)	300	250
F.W. (g/mol);	447.4	447.4
Space group; Z	P-3m1 (No.164); 1	P-1 (No. 2); 1
a (Å)	3.940(2)	3.954(4)
a (Å)	3.940(2)	6.649(7)
c (Å)	5.406(4)	14.458(14)
α (°)	90	98.11(4)
β (°)	90	92.53(3)
γ (°)	120	107.10(3)
$V(\text{Å}^3)$	72.7(1)	358.2(6)
Absorption correction	Numerical	Numerical
Extinction coefficient	None	None
θ range (deg)	4.27–45.58	3.248–32.170
No. reflections; R_{int}	546; 0.0512	2779; 0.0958
No. independent reflections	117	2025
No. parameters	6	70
R_1; wR_2 (all I)	0.0413; 0.0700	0.0728; 0.1540
Goodness of fit	1.058	1.146
Diffraction peak and hole (e^-/Å^3)	3.131;–2.139	6.684;–5.208

are typically 5 mm on a side and 1 mm in thickness, as shown in Fig. 1(a). X-ray diffraction (XRD) (Panalytical Empyrean) of powdered single crystals indicates the trigonal crystal structure. As indicated in Fig. 1(b), all observed peaks can be indexed by a single phase, suggesting that our as-grown crystals are phase pure. To obtain more detailed structural information, single-crystal XRD measurements were carried out using Bruker Apex II diffractometer equipped with Mo $K\alpha$ radiation ($\lambda = 0.71073$ Å). The data were collected to determine the crystal structures over a range in temperature in the following sequence: 300 K $\Rightarrow$ 250 K $\Rightarrow$ 90 K $\Rightarrow$ 300 K $\Rightarrow$ 350 K $\Rightarrow$ 300 K. Numerical absorption corrections were accomplished with XPREP, which is based on face-indexed absorption [24]. The crystal structures were solved

with the aid of the SHELXTL package [24] using direct methods (SHELXS-97) and were refined by full-matrix least-squares on F^2 [25]. The disorder refinements on Ir and Te sites show no vacancies or mixtures on either site. Thus, we interpret these results as strong evidence that our single crystals are stoichiometric IrTe$_2$. The electrical resistivity, Hall effect, and specific heat were measured using a Quantum Design Physical Property Measurement System (PPMS-14 T) with temperature range between 1.8 K and 400 K. A four-probe method is employed to measure the ab plane, c axis, and Hall resistivities. The Hall resistivity measurements were performed at fixed temperatures for both positive and negative magnetic fields in order to extract the asymmetric component with respect to the field. Magnetic susceptibility measurements were performed in a Quantum Design Magnetic Property Measurement System (MPMS -7T).

III. RESULTS AND DISCUSSION

As depicted in Fig. 1(c), IrTe$_2$ adopts the trigonal symmetry with space group $P\bar{3}m1$(No. 164) at 300 K before (start) and after thermal cycling (end), consistent with the crystal morphology. Detailed crystal structural information at 300 K and 250 K are presented in Tables I and II. The structure refinement results in lattice parameters $a = b = 3.940(2)$ Å and $c = 5.406(4)$ Å with atomic distances indicated in Fig. 1(c). These parameters are very close to those obtained previously for IrTe$_2$ [7,8,21]. As shown in Fig. 1(d), Bragg reflections from IrTe$_2$ reveal extremely sharp spots with a hexagonal distribution at room temperature. Upon cooling to 250 K, we observe a larger number of Bragg reflections than at room temperature. At $T = 250$ K, our refinement indicates that the structure changes to a triclinic [$P\bar{1}$ (No. 2)] symmetry with $a = 3.954(4)$ Å,$b = 6.649(7)$ Å,$c = 14.458(14)$ Å,$\alpha = 98.11(4)°,\beta = 92.53(3)°$, and $\gamma = 107.10(3)°$ (see Table I). This is very close to that obtained previously for temperatures below T_{S1} [20]. The schematic crystal structure based on our refinement of these data is shown in Fig. 1(g). Upon further cooling to 90 K, the Bragg reflections [Fig. 1(e)] are irregular and with even larger density of spots than that at 250 K,

TABLE II. Atomic coordinates and equivalent isotropic displacement parameters of IrTe$_2$. U_{eq} is defined as one-third of the trace of the orthogonalized U_{ij} tensor (Å^2).

| Atom	Wyckoff	Occupancy	x	y	z	U_{eq}
300 K						
Ir	1a	1	0	0	0	0.0077(3)
Te	2d	1	2/3	1/3	0.7469(2)	0.0091(4)
250 K						
Atom	Wyckoff	Occupancy	x	y	z	U_{eq}
Ir$_1$	1c	1	0	1/2	0	0.0058(10)
Ir$_2$	2i	1	0.1402(8)	0.9287(5)	−0.4106(2)	0.0063(8)
Ir$_3$	2i	1	−0.4251(9)	0.7131(6)	−0.2032(2)	0.0061(8)
Te$_1$	2i	1	0.2028(9)	0.9780(9)	−0.2221(3)	0.0064(11)
Te$_2$	2i	1	−0.3655(9)	0.7717(8)	−0.0165(3)	0.0060(12)
Te^3	2i	1	−0.0549(9)	0.4451(9)	−0.1842(3)	0.0056(11)
Te^4	2i	1	0.5171(9)	0.6579(9)	−0.3878(3)	0.0078(12)
Te^5	2i	1	0.2175(13)	0.8001(8)	−0.5884(3)	0.0059(12)
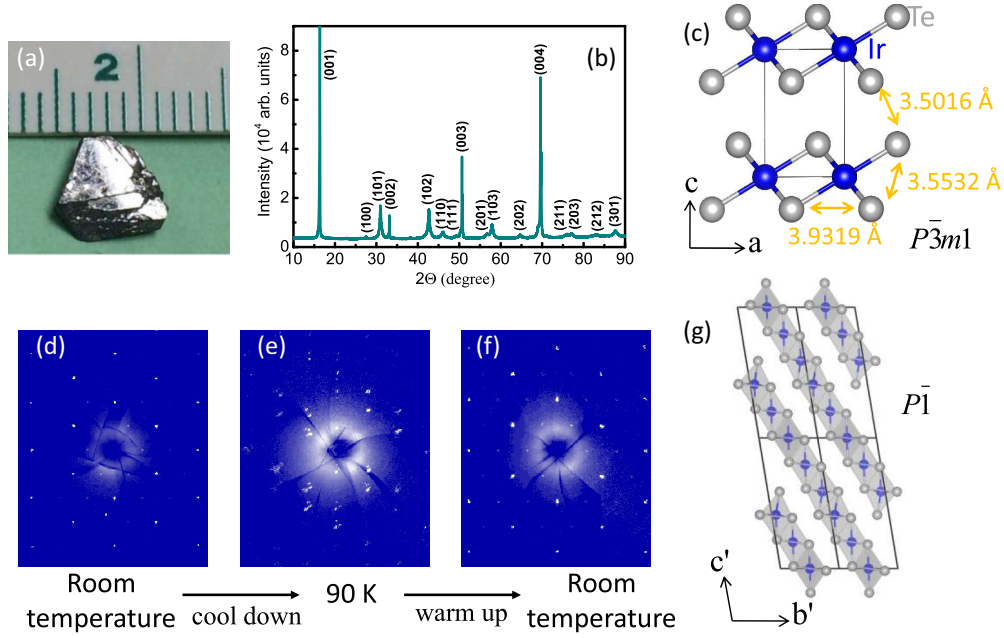
FIG. 1. (a) Photograph of an $IrTe_2$ single crystal. (b) Room-temperature powder XRD patterns of $IrTe_2$. (c) Crystal structure of $IrTe_2$ at 300 K, Te-Te distances are indicated. (d–f) Single-crystal x-ray diffraction procession images in the ($H\,K\,0$) reciprocal plane at 300 K (d), 90 K (e), and 300 K (f) after the thermal cycling. (g) The structure of $IrTe_2$ at 250 K.

making refinement difficult. By investigating the detailed electron density maps, partial dimerization was observed through the presence of "extra" domains, while the overall structure remains intact. Remarkably, the crystal resumes its high-temperature structure after the thermal cycling as shown in Fig. 1(f). This is consistent with the reproducibility of physical properties through thermal cycling.

Figure 2(a) shows the temperature dependence of the in-plane electrical resistivity (ρ_{ab}) of $IrTe_2$ between 3 and 400 K. Similar to previous observations [21,22], ρ_{ab} exhibits standard metallic behavior at high temperatures, i.e., decreasing linearly with decreasing temperature. Upon cooling from 400 K there is a sharp rise in ρ_{ab} occurring at $T_{S1} = 283$ K. With further cooling, a second jump in ρ_{ab} emerges at $T_{S2} = 167$ K. These resistivity jumps are likely the result of the structure transitions apparent in the structure refinements. The latter transition is much less pronounced during the warming process, whereas the steep increase at T_{S1} is even sharper than when cooling. The result is a large thermal hysteresis between 150 and 283 K. Note that this hysteresis loop is different from that reported earlier [8,12] in which there is no transition observed at T_{S2} and the transition at T_{S1} upon warming is larger than when cooling. According to Refs. [21] and [22], the absence of a second phase transition at T_{S2} is caused by a poor sample quality. This is consistent with our structural data, indicating that our single crystals are of high quality.

The anomalies at T_{S1} and T_{S2} are also observed in the out-of-plane resistivity (ρ_c) of $IrTe_2$ displayed in Fig. 2(b). Overall, ρ_c has a similar temperature profile as ρ_{ab}. However, differences are observed between the in- and out-of-plane resistivities including (1) ρ_c is more than a factor of 100 times larger than ρ_{ab}, and (2) there is a hysteresis in the temperature dependence of ρ_c, i.e., it is larger upon warming above T_{S1} than we observed in our initial data taken upon cooling from

400 K. These differences are more apparent when plotting the ratio ρ_c/ρ_{ab} as in Fig. 2(c). Here we observe that ρ_c/ρ_{ab} is ∼350 at 400 K, increasing to ∼730 when cooling to 4 K. Additionally, we observe hysteresis in this ratio above T_{S2}, which is enhanced further above T_{S1} where $\rho_c/\rho_{ab} \approx 430$ at 400 K. This ratio is much larger than that reported in samples that do not display the structural transition at T_{S2} [13]. Naively, the large ρ_c/ρ_{ab} is rather unexpected, since the interlayer Te-Te distance [3.5016(6) Å] is shorter than that within the ab plane [3.5532(6) Å and 3.9319(4) Å] at room temperature, as indicated in Fig. 1(c). This implies that the interlayer bonding is covalent instead of the weaker van der Waals type [21]. We conclude that the poor electrical conduction for out-of-plane charge transport is due to more subtle electronic structure effects. The small in-plane resistivity [$\rho_{ab}(300\,K) \approx 40\,\mu\Omega\,cm$] suggests metallic Ir-Te bonding within the layer, resulting in much higher conductivity than the interlayer conductivity. Both first-principles calculations and experiments suggest a change in the electronic structure, becoming far more two-dimensional below the structural transition temperature T_{S1} due to the partial dimerization of Ir-Ir and Te-Te [15,20,26,27]. The enhanced ρ_c/ρ_{ab} below T_{S1} and T_{S2} we observed confirms such a trend.

In prototypical metallic systems the itinerant electrons give rise to a positive magnetic susceptibility with a magnitude proportional to the density of states (DOS) at the Fermi level. Figures 2(d) and 2(e) show the temperature dependence of the magnetic susceptibilities (χ_{ab}, χ_c) of $IrTe_2$ measured by applying a magnetic field of $\mu_0 H = 1$ T along the ab plane and the c axis, respectively. Several features are worth noting: (1) χ_{ab} and χ_c display a similar temperature dependence, with both exhibiting hysteresis with thermal cycling; (2) χ_{ab} and χ_c become increasingly diamagnetic below each of the structural transitions (T_{S1} and T_{S2}); and (3) both χ_{ab}
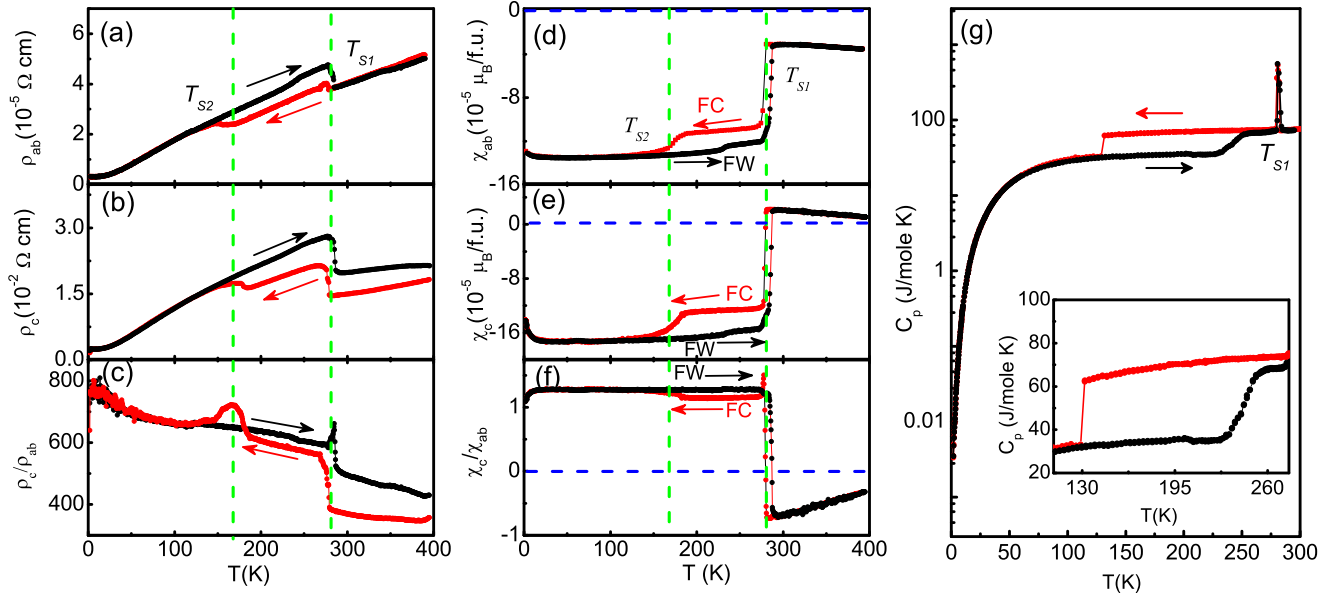
FIG. 2. IrTe$_2$: Temperature dependence of the in-plane resistivity, ρ_{ab} (a), the out-of-plane resistivity, ρ_c (b), ρ_c/ρ_{ab} (c), the magnetic susceptibility for fields oriented in plane, χ_{ab} (d), and out-of-plane, χ_c (e), χ_c/χ_{ab} (f), and the specific heat C_p (g). The inset in (g) is C_p between 120 and 280 K. Data displayed for both cooling (red) and warming (black) conditions.

and χ_c decrease with increasing T above T_{S1} with $\chi_{ab} < 0$ and $\chi_c > 0$. While a positive χ_c indicates a dominant Pauli susceptibility above T_{S1}, the observation of a negative χ_{ab} is unusual for a metallic system. This implies that the positive contribution from itinerant electrons to χ_{ab} is smaller than the diamagnetic core contribution in IrTe$_2$. In heavy metals, such as Bi, diamagnetism is also related to interband interactions and spin-orbit coupling [28]. The enhancement of the diamagnetism at T_{S1} and T_{S2} is likely the result of interband interactions connected to the charge transfer between Ir and Te [21] causing electron localization. The inclusion of strong spin-orbit coupling is expected to further enhance the core diamagnetism [28].

To help understand the nature of anomalies at T_{S1} and T_{S2}, we have measured the specific heat (C_p) of our crystals. Figure 2(g) displays the temperature dependence of C_p plotted on a logarithmic scale. Similar to a previous observation [12], there is an extremely sharp peak at T_{S1} observed in both the cooling and warming processes, confirming the first-order nature of this transition. In addition, there is steep decrease of C_p at ~130 K through cooling [see the inset of Fig. 2(g)] that occurs at the temperature where the hysteresis loop closes for both the resistivity and magnetic susceptibility [see Figs. 2(a)–2(f)]. This indicates that there is true first-order phase transition at T_{S2}. As can be seen in the inset of Fig. 2(g), there is a clear hysteresis loop in C_p, similar to that seen in the resistivity and magnetic susceptibility.

The observation of two structural phase transitions in our IrTe$_2$ is truly remarkable, because most previous investigations indicate only a single phase transition with no indication of superconductivity at low T. This transition may be absent when there is significant Ir deficiency, Ir$_{1-x}$Te$_2$. In addition, in Ir$_{1-x}$Te$_2$, superconductivity emerges at $T_c \approx 2.5$ K [19]. As shown in Fig. 3(a), both ρ_{ab} and ρ_c of IrTe$_2$ display

a steep decrease below ~2.5 K, indicating the initiation of a superconducting phase transition. Correspondingly, the magnetic susceptibility displays a steep diamagnetic drop at this same temperature, as can be seen in the inset of Fig. 3(a). This indicates that there is indeed a superconducting transition at $T_c = 2.5$ K, although the small change in the magnetic susceptibility apparent above 1.8 K leaves the open possibility of either a surface or filamentary superconducting state. However, evidence for bulk superconductivity is obtained from specific heat presented in Fig. 3(b) as C_p/T versus T^2. At T_c there is a specific heat jump of magnitude $\Delta C_p/T_c \approx 1.5$ mJ/mol K^2. In addition, this specific heat anomaly is completely suppressed by the application of $\mu_0 H = 1$ T magnetic field. By fitting the normal-state specific heat with the standard form for a metal, $\frac{C_p(T)}{T} = \gamma + \beta T^2$, we obtain the Sommerfeld coefficients $\gamma = 1.8$ mJ mol^{-1}K^{-2} and $\beta = 0.60$ mJ mol^{-1} K^{-4}. Thus, the ratio $\frac{\Delta C_p}{\gamma T_c} \approx 0.83$, is substatially smaller than the BCS value of 1.43 expected for superconductors in the weak-coupling limit. This suggests that the superconducting state is a bulk property of this material; however, it is not shared by the entire volume of our sample. This is consistent with scanning tunneling microscopy (STM) measurements on IrTe$_2$, which show a phase separation between superconducting and normal metallic behavior associated with different charge order structures within the samples [29]. To elucidate the nature of the superconducting transition in our single-crystal samples, physical property measurements down to much lower temperatures are necessary. In particular, microscopic approaches such as STM will confirm if the system contains both the superconducting and normal metallic domains.

In the usual model for the specific heat of metals used above to fit our data above T_c, one term (γT) measures the electronic contribution while the second term (βT^2) describes
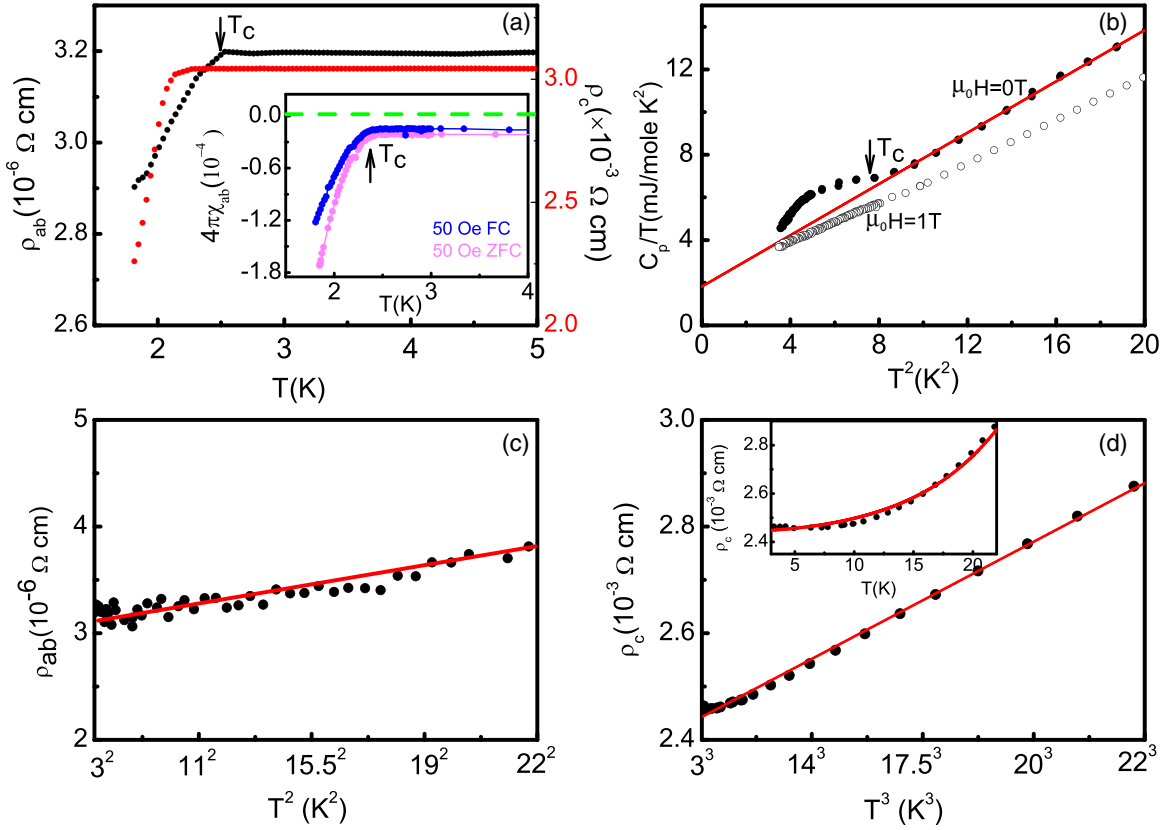
FIG. 3. (a) Low-temperature ρ_{ab} (black, left axis) and ρ_c (red, right axis). The inset is the temperature dependence of the in-plane magnetic susceptibility χ_{ab} taken at 50 Oe. (b) Specific heat, C_p, plotted as C_p/T vs T^2 at zero field, H, and 1 Tesla. The solid line represents fit of the form $C_p/T = \gamma + \beta T^2$ to the data between 3 and 4.5 K. (c) ρ_{ab} (T) plotted as a function of T^2 between 3 and 22 K. The solid line denotes a fit of the form $\rho_{ab} = \rho_{ab0} + A_{ab}T^2$ to the data. (d) ρ_c (T) plotted as a function of T^3 between 3 and 22 K. The solid line illustrates that $\rho_c \propto T^3$. Inset demonstrates fit of the form $\rho_c = \rho_{c0} + A_c T^2 + B_c T^5$ to $\rho_c(T)$ data. The solid curve demonstrates the resulting best fit.

the phonon contribution. The Debye temperature Θ_D can be estimated from β using $\Theta_D = (12\pi^4 N R/5\beta)^{1/3}$, where $N = 3$ for IrTe$_2$ and R is the universal gas constant. Here we find $\Theta_D = 213$ K, consistent with a previous measurement [9]. However, the value of γ that results from our fit is significantly smaller than other reports [9,12]. The small γ value indicates a small electron DOS at the Fermi surface of IrTe$_2$. This small γ and the formation of additional electron and hole pockets [22] imply weaker electron-electron correlation below T_{S2}, consistent with first-principles calculations [20]. Information about the electron-electron correlation strength can also be obtained from low-temperature transport properties. In Fig. 3(c), the in-plane resistivity is replotted as ρ_{ab} versus T^2 between 3 K and 22 K. The linear behavior indicates that the data can be described by the Fermi liquid form $\rho_{ab} = \rho_{ab0} + A_{ab}T^2$. The fit of our data to this form results in $\rho_{ab0} = 2.97\ \mu\Omega$ cm, and $A_{ab} = 1.2 \times 10^{-3}\ \mu\Omega$ cm/K^2. The quadratic temperature dependence of ρ_{ab} indicates that electron-electron scattering is the dominant temperature-dependent scattering mechanism for electrical transport within the ab plane below 22 K. While the Kadowaki-Woods (KW) ratio $R_{KW} = A_{ab}/\gamma^2$ is often used to characterize the electron-electron correlation strength, it is not expected to be suitable to characterize layered materials [30]. Therefore, the large $R_{KW} \approx 4 \times 10^{-4} \mu\Omega$ cm mol^2 K^2(mJ)$^{-2}$

for IrTe$_2$ may not be the reflection of strong electron-electron correlation. In contrast, ρ_c exhibits a different behavior with the temperature dependence consistent with $\rho_c \propto T^3$ [see Fig. 3(d)]. To model this behavior, we fit ρ_c using a simple model of electron-electron scattering along with electron-phonon scattering $\rho_c = \rho_{c0} + A_c T^2 + B_c T^5$, where ρ_{c0}, A_c, and B_c are constants. The best fit to our data between 3 and 22 K results in $\rho_{c0} = 2.44$ mΩ cm, $A_c = 0.51\ \mu\Omega$ cm/K^2, and $B_c = 3.4 \times 10^{-5}\ \mu\Omega$ cm/K^5 [see the solid line in the inset of Fig. 3(d)]. This indicates that, in addition to electron-electron scattering (T^2 dependence), the electron-phonon scattering (T^5 dependence) has to be taken into account to describe the out-of-plane electrical transport.

With multiple phase transitions that cause electronic structure reconstructions, the Hall effect of IrTe$_2$ should be informative. Figures 4(a) and 4(b) show the field dependence of the Hall resistivity (ρ_{xy}) of IrTe$_2$ at different temperatures through cooling and warming, respectively. At $T > T_{S1}$, ρ_{xy} reveals an excellent linear H dependence between 0 and 14 Tesla with a negative slope. Upon cooling, below T_{S1}, ρ_{xy} decreases significantly with a slight nonlinearity at high fields [see Fig. 4(a)]. With further cooling ρ_{xy} recovers somewhat until $T < T_{S2}$, where it increases eventually so that it is almost the same value below 100 K as it was at 300 K. The trend
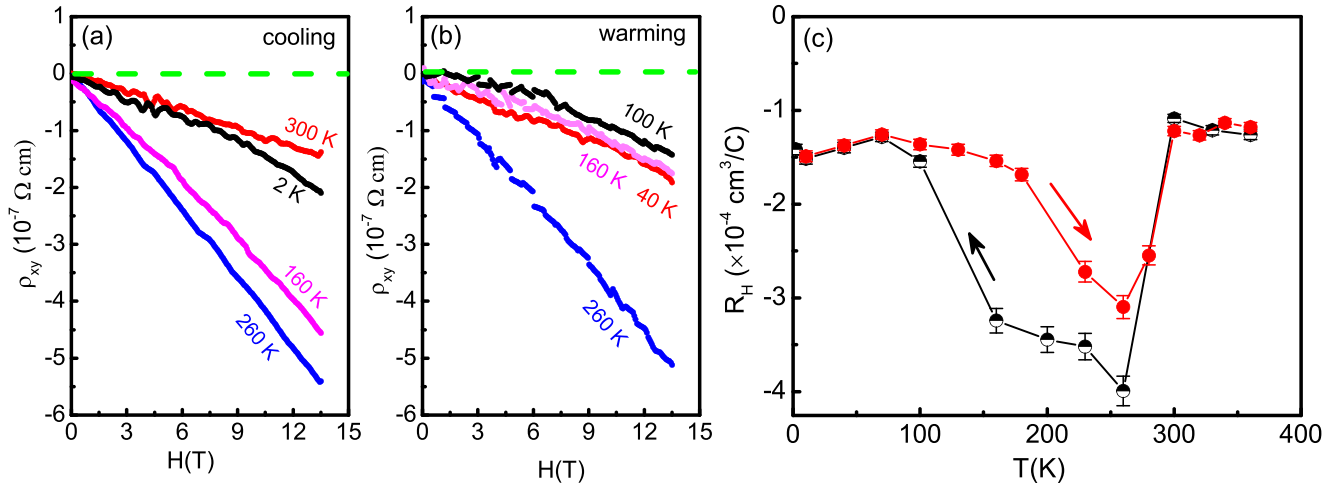
FIG. 4. Field dependence of the Hall resistivity ρ_{xy} at indicated temperatures through cooling (a) and warming (b). (c) Temperature dependence of the Hall coefficients R_H found from linear fits of the $\rho_{xy}(H)$ data for the cooling and warming processes.

is comparable upon warming [see Fig. 4(b)] with a similar hysteresis apparent in ρ_{xy} as in ρ, χ, and C_p. The Hall coefficient R_H found from the slope of ρ_{xy}(H) is displayed as function of T for both cooling and warming in Fig. 4(c). Note that the Hall coefficient is negative at all temperatures, indicating that charge carriers are predominantly electrons. This is rather different from a previous publication [11], which reports a sign change of R_H from positive at high temperatures to negative below ~90 K. In particular, our $R_H(T)$ exhibits a large change at both T_{S1} and T_{S2}, confirming a significant modification of the electronic structure that is associated with both of these phase transitions. The increase of the magnitude of R_H for temperatures between T_{S1} and T_{S2} indicates a reduction of charge carrier density in the intermediate phase. Using the simple Drude model, we estimate that the carrier density $n = \frac{1}{e|R_H|} \sim 5 \times 10^{22}\,\mathrm{cm}^{-3}$ above T_{S1} and $n \approx 1.2 \times 10^{22}\,\mathrm{cm}^{-3}$ below T_{S1}. Since there is no indication of the opening of an energy gap at the Fermi surface [31], we attribute the decrease of carrier concentration to the reconstruction of the Fermi surface across T_{S1}, as confirmed by optical spectroscopy measurements [12] and consistent with the changes in crystal structure determined from our single-crystal XRD [20]. Remarkably, the increase in the magnitude of R_H below T_{S2} suggests that the carrier concentration recovers somewhat after two consecutive structural transitions. The larger charge-carrier concentration at low temperatures in our samples, which is different from those reported earlier that did not display the structural phase transition at T_{S2}, may be closely related to the observation of superconductivity at 2.5 K. In earlier reports it was argued that chemical substitutions using Tm in $\mathrm{Ir}_{1-x}Tm_x\mathrm{Te}_2$ ($Tm = \mathrm{Pt,Pd,Rh}$) [8–10] and Cu intercalation [11] are effectively electron doping, suggesting that a higher charge density is a requirement for superconductivity in this system. From this point of view, we can essentially tie together the phase transition at T_{S2} and the emergence of superconductivity in our crystals, as our Hall data demonstrate the recovery of a larger carrier density with cooling through T_{S2}, creating the necessary conditions for superconductivity.

However, much remains to be understood considering the emergence of superconductivity in Ir-deficient $\mathrm{Ir}_{1-x}\mathrm{Te}_2$ [19]. Naively, Ir deficiency would be equivalent to hole doping, resulting in even lower electron carrier density than the stoichiometric case. What is common between superconducting $\mathrm{Ir}_{1-x}\mathrm{Te}_2$ and $\mathrm{Ir}_{1-x}Tm_x\mathrm{Te}_2$ is the absence of the structural transition. While superconducting $\mathrm{Ir}_{1-x}\mathrm{Te}_2$ crystallizes a monoclinic structure [19], theoretical calculations indicate that electron-phonon coupling is too weak to trigger superconductivity [32]. Recent STM investigation reveals both a stripe phase and hexagonal phase at the surface, and the latter hosts a superconducting state [29]. To elucidate the superconductivity-structure relationship in our stoichiometric IrTe_2 crystals where two phase transitions are readily apparent, it is necessary to perform experiments such as STM.

IV. CONCLUSION

In summary, we have investigated the structural, electrical, magnetic, and thermodynamic properties of high-quality singlecrystalline IrTe_2, which forms in a trigonal structure at room temperature but triclinic at lower temperatures. Different from all previous reports, we observe three consecutive phase transitions, two of which are structural ($T_{S1} \approx 283$ K and $T_{S2} \approx 167$ K) and one superconducting ($T_c \approx 2.5$K) through structural, electrical, magnetic, and thermodynamic property measurements. While there is little magnetic anisotropy, a large electrical resistivity anisotropy exists which increases with decreasing temperature. The T^2 dependence of in-plane resistivity reflects the Fermi-liquid behavior at low temperatures while the dramatic changes of Hall coefficient indicate electronic structure reconstructions at both T_{S1} and T_{S2} which are reflected in the behavior of the electrical resistivity and magnetic susceptibility. A comparison with earlier work on samples that did not display a transition at T_{S2}, along with samples that were effectively electron doped via chemical substitution or intercalation, indicates that the higher carrier density associated with the low-temperature

phase in our samples may be essential for the emergence of superconductivity. We call for further experimental and theoretical investigations regarding how the charge ordering and related crystallographic structure changes can trigger the formation of Cooper pairs in $IrTe_2$.

[1] R. Friend and A. Yoffe, Adv. Phys. **36**, 1 (1987).

[2] T. Yokoya, T. Kiss, A. Chainani, S. Shin, M. Nohara, and H. Takagi, Science **294**, 2518 (2001).

[3] B. Sipos, A. F. Kusmartseva, A. Akrap, H. Berger, L. Forró, and E. Tutiš, Nature Mater. **7**, 960 (2008).

[4] T. Valla, A. V. Fedorov, P. Johnson, P. Glans, C. McGuinness, K. Smith, E. Andrei, and H. Berger, Phys. Rev. Lett. **92**, 086401 (2004).

[5] S. V. Borisenko, A. A. Kordyuk, V. B. Zabolotnyy, D. S. Inosov, D. Evtushinsky, B. Büchner, A. N. Yaresko, A. Varykhalov, R. Follath, W. Eberhardt, L. Patthey, and H. Berger, Phys. Rev. Lett. **102**, 166402 (2009).

[6] E. Morosan, H. Zandbergen, B. Dennis, J. Bos, Y. Onose, T. Klimczuk, A. Ramirez, N. Ong, and R. Cava, Nat. Phys. **2**, 544 (2006).

[7] C. J. Raub, V. Compton, T. Geballe, B. Matthias, J. Maita, and G. Hull, J. Phys. Chem. Solids **26**, 2051 (1965).

[8] J. J. Yang, Y. J. Choi, Y. S. Oh, A. Hogan, Y. Horibe, K. Kim, B. Min, and S. Cheong, Phys. Rev. Lett. **108**, 116402 (2012).

[9] S. Pyon, K. Kudo, and M. Nohara, J. Phys. Soc. Jpn. **81**, 053701 (2012).

[10] K. Kudo, M. Kobayashi, S. Pyon, and M. Nohara, J. Phys. Soc. Jpn. **82**, 085001 (2013).

[11] M. Kamitani, M. Bahramy, R. Arita, S. Seki, T. Arima, Y. Tokura, and S. Ishiwata, Phys. Rev. B **87**, 180501 (2013).

[12] A. Fang, G. Xu, T. Dong, and N. L. Wang, Sci. Rep. **3**, 1153 (2013).

[13] Y. S. Oh, J. J. Yang, Y. Horibe, and S.-W. Cheong, Phys. Rev. Lett. **110**, 127209 (2013).

[14] D. Ootsuki, Y. Wakisaka, S. Pyon, K. Kudo, M. Nohara, M. Arita, H. Anzai, H. Namatame, M. Taniguchi, N. L. Saini, and T. Mizokawa, Phys. Rev. B **86**, 014519 (2012).

[15] D. Ootsuki, S. Pyon, K. Kudo, M. Nohara, M. Horio, T. Yoshida, A. Fujimori, M. Arita, H. Anzai, H. Namatame, M. Taniguchi, N. L. Saini, and T. Mizokawa, J. Phys. Soc. Jpn. **82**, 093704 (2013).

[16] N. Matsumoto, K. Taniguchi, R. Endoh, H. Takano, and S. Nagata, J. Low Temp. Phys. **117**, 1129 (1999).

[17] Y. Qi, S. Matsuishi, J. Guo, H. Mizoguchi, and H. Hosono, Phys. Rev. Lett. **109**, 217002 (2012).

[18] L. Li, T. F. Qi, L. S. Lin, X. X. Wu, X. T. Zhang, K. Butrouna, V. S. Cao, Y. H. Zhang, Jiangping Hu, S. J. Yuan, P. Schlottmann, L. E. De Long, and G. Cao, Phys. Rev. B **87**, 174510 (2013).

[19] X. Li, J.-Q. Yan, D. J. Singh, J. B. Goodenough, and J.-S. Zhou, Phys. Rev. B **92**, 155118 (2015).

[20] G. L. Pascut, K. Haule, M. J. Gutmann, S. A. Barnett, A. Bombardi, S. Artyukhin, T. Birol, D. Vanderbilt, J. J. Yang, S.-W. Cheong, and V. Kiryukhin, Phys. Rev. Lett. **112**, 086402 (2014).

[21] K. T. Ko, H.-H. Kim, J.-J. Yang, S.-W Cheong, M. J. Eom, J. S. Kim, R. Gammag, K. S. Kim, H. S. Kim, T. H. Kim *et al.*, Nat. Commun. **6**, 7342 (2015).

[22] M. J. Eom, K. Kim, Y. J. Jo, J. Yang, E. S. Choi, B. I. Min, J.-H. Park, S.-W. Cheong, and J. S. Kim, Phys. Rev. Lett. **113**, 266406 (2014).

[23] H. Cao, B. C. Chakoumakos, X. Chen, J. Yan, M. A. McGuire, H. Yang, R. Custelcean, H. Zhou, D. J. Singh, and D. Mandrus, Phys. Rev. B **88**, 115122 (2013).

[24] G. Sheldrick, Inc., XPREP, Madison, WI, USA, 2000.

[25] G. Sheldrick, SHELXTL, Germany, 1997.

[26] T. Toriyama, M. Kobori, T. Konishi, Y. Ohta, K. Sugimoto, J. Kim, A. Fujiwara, S. Pyon, K. Kudo, and M. Nohara, J. Phys. Soc. Jpn. **83**, 033701 (2014).

[27] D. Ootsuki, T. Toriyama, S. Pyon, K. Kudo, M. Nohara, K. Horiba, M. Kobayashi, K. Ono, H. Kumigashira, T. Noda, T. Sugimoto, A. Fujimori, N. L. Saini, T. Konishi, Y. Ohta, and T. Mizokawa, Phys. Rev. B **89**, 104506 (2014).

[28] F. Buot and J. McClure, Phys. Rev. B **6**, 4525 (1972).

[29] H. S. Kim, S. Kim, K. Kim, B. I. Min, Y.-H. Cho, L. Wang, S.-W. Cheong, and H. W. Yeom, Nano Lett. **16**, 4260 (2016).

[30] A. Jacko, J. Fjærestad, and B. Powell, Nat. Phys. **5**, 422 (2009).

[31] K. Kim, S. Kim, K.-T. Ko, H. Lee, J.-H. Park, J. Yang, S.-W. Cheong, and B. Min, Phys. Rev. Lett. **114**, 136401 (2015).

[32] B. Li, G. Huang, J. Sun, and Z. Xing, Sci. Rep. **4**, 6433 (2014).